Nanoscale Advances

ROYAL SOCIETY OF CHEMISTRY

PAPER

View Article Online
View Journal | View Issue

Cite this: *Nanoscale Adv.*, 2021, **3**, 2007

Effect of pomelo seed-derived carbon on the performance of supercapacitors†

Zhenyao Yin,‡[a] Yaping Xu,‡[a] Jinggao Wu[c] and Jing Huang *[ab]

Received 18th September 2020
Accepted 12th February 2021

DOI: 10.1039/d0na00778a

rsc.li/nanoscale-advances

Electrochemical ultracapacitors derived from green and sustainable materials could demonstrate superior energy output and an ultra-long cycle life, which could contribute to next-generation applications. Herein, we utilize pomelo seeds, a bio-waste from pomelo, in high-energy and high-power supercapacitors by a facile low-cost pyrolysis and activation method. The as-synthesized hierarchically porous carbon is surface-engineered with a large quantity of nitrogen and sulfur heteroatoms to give a high specific capacitance of ~845 F g^{-1} at 1 A g^{-1}. An ultra-high stability of ~93.8% even after 10 000 cycles (10 A g^{-1}) is achieved at room temperature. Moreover, a maximum energy density of ~85 W h kg^{-1} at a power density of 1.2 kW kg^{-1} could be achieved in 1.2 V aqueous symmetrical supercapacitors. The results provide new insights that will be of use in the development of high-performance, green supercapacitors for advanced energy storage systems.

1. Introduction

The depletion of fossil fuels and the increasingly serious environmental problems have caused great concerns for developing high-performance energy storage devices. Among the various energy storage devices, supercapacitors are becoming a hot spot of research and they make up the difference between batteries and conventional capacitors owing to their great advantages including high power density, high rates of charge/discharge, and long cycle life.[1–5] Generally, supercapacitors can be classified into three categories according to the capacitor source: electrical double layer capacitors (EDLCs), pseudo-capacitors and hybrid capacitors.[6–8] In EDLCs, the capacitance is derived from the pure electrostatic charge accumulation at the electrode and electrolyte interface.[9] On account of this, the electrode becomes an important factor affecting the performance. Further, the performance of the electrode mainly depends on the electrode material. Therefore, the choice of electrode material is the key step for capacitors.

At present, porous carbon materials with a micro-carbon pore structure, such as activated carbon (AC),[10] carbon aerogels[11] and carbon nanotubes,[12] are widely used as electrode materials for EDLCs by virtue of their high conductivity and electrochemical stability. Among these carbon materials, activated carbon is considered as the most promising carbon material due to its simple preparation process, low equipment requirements and high specific surface area.[13] However, the activated carbon prepared by the conventional process mainly uses expensive and non-renewable materials such as coal, petroleum and its derivatives as raw materials.[14] Therefore, it is urgent to explore a new material to prepare AC. Compared with traditional fossil fuels, biomass materials have the advantages of renewability, low cost, environmental friendliness and abundant carbon sources.[15] At present, a wide variety of waste biomass materials are used as carbon precursors for the preparation of porous activated carbon, such as egg white,[16] seaweed,[17] raw wood,[18] rape pollen,[19] rice hulls,[20] and waxberry.[21] Moreover, these carbonaceous materials as electrode materials for supercapacitors have exhibited superior performance.[22,23]

Pomelo belongs to the genus citrus and is widely distributed in the south of China's Yangtze River and Southeast Asia. Except for the sarcocarp of pomelo, pomelo peel and valves as well as its seeds are discarded as biomass waste. Apart from this, the various components of pomelo seeds are rich in carbon, such as protein, fiber and fatty acids. Based on this, our target is to use pomelo seeds as a precursor to prepare electrochemical materials for supercapacitors. This not only enriches the selection of electrode material precursors, but also realizes the economic value maximization of waste pomelo seeds.

In this study, we develop a high-energy and robust supercapacitor with waste pomelo seed derived activated carbon as the electrode material by means of high temperature pre-carbonization

[a]*State Key Laboratory of Silkworm Genome Biology, Key Laboratory of Sericultural Biology and Genetic Breeding, Ministry of Agriculture and Rural Affairs, College of Sericulture, Textile and Biomass Sciences, Southwest University, Chongqing 400715, PR China. E-mail: hj41012@163.com*

[b]*Institute for Clean Energy & Advanced Materials, Faculty of Materials and Energy, Southwest University, Chongqing 400715, P. R. China*

[c]*Key Laboratory of Rare Earth Optoelectronic Materials & Devices, College of Chemistry and Materials Engineering, Huaihua University, Huaihua 418000, PR China*

† Electronic supplementary information (ESI) available. See DOI: 10.1039/d0na00778a

‡ Equal contribution to this work.

and KOH activation (Scheme 1). We have explored the conditions, and characterized the structure as well as evaluated its application prospect as the electrode material of supercapacitors.

2. Experimental section

2.1 Materials and methods

2.1.1 Materials and reagents. Pomelos were purchased from a local market in China and the pomelo seeds were collected after removing the edible portions. Nafion solution, acetylene black, poly(tetrafluoroethylene) (PTFE), and ethanol were purchased from Sigma-Aldrich. Potassium hydroxide (KOH) and all others reagents were obtained from Adamas-Beta®. All chemicals were used without further purification.

2.1.2 Preparation of pomelo seed-derived activated carbon (PSAC). Activated carbons were prepared by pyrolysis using pomelo seeds and KOH as raw materials. First, the pomelo seeds were heated in a tube furnace under an argon atmosphere to 400 °C with a heating rate of 5 °C min^{-1}, and then the temperature was held for 1 hour. Then, it was further heated to 800 °C at the same heating rate and cooled down to room temperature after 2 hours of heat preservation. The obtained carbon was named PSC. Next, PSC and KOH with a mass ratio of 1 : 1 were thoroughly ground in an agate mortar. After grinding, the same pyrolysis process was carried out in a tube furnace according to the preparation of PSC. Finally, the obtained carbon was named PSAC-3. For comparison, different mass ratios of PSC and KOH (2 : 1; 3 : 2, 2 : 3; 1 : 2) were also investigated under the above process. The samples were denoted as PSAC-1, PSAC-2, PSAC-4 and PSAC-5. In addition, PSAC-6 and PSAC-7 were prepared at 700 and 900 °C in accordance with a similar procedure to that for PSAC-3. In the whole process, all carbonized samples were drastically washed with diluted HCl and deionized water, and then dried at 80 °C for 12 h.

2.2 Characterization

The XRD patterns of all samples were recorded using powder X-ray diffraction (Shimadzu XRD-7000). The surface morphology and structure of the samples were observed using scanning electron microscopy (FESEM, JSM-7800F) and transmission electron microscopy (TEM, JEOL 2100). Nitrogen sorption isotherms were obtained using an Autosorb-1 (Quantachrome Instruments). The specific surface area was calculated by the modified Brunauer–Emmett–Teller (BET) method. The pore size distributions and the pore volume were analyzed from the adsorption branch isotherms by the density functional theory (DFT) method. Moreover, the total pore volume (V_t) was estimated from the amount adsorbed at a relative pressure P/P_0 of 0.990. The micropore volume (V_{mic}) and micropore surface area (S_{mic}) were determined by t-plot theory. Raman spectra were acquired with a Jobin-Yvon HR 800 spectrometer. X-ray photoelectron spectroscopy (XPS) measurements were performed on a Thermo Fisher Scientific (Escalab 250xi, USA). Fourier transform infrared (FT-IR) spectra were recorded on a Thermo Scientific Nicolet iS 50 spectrometer.

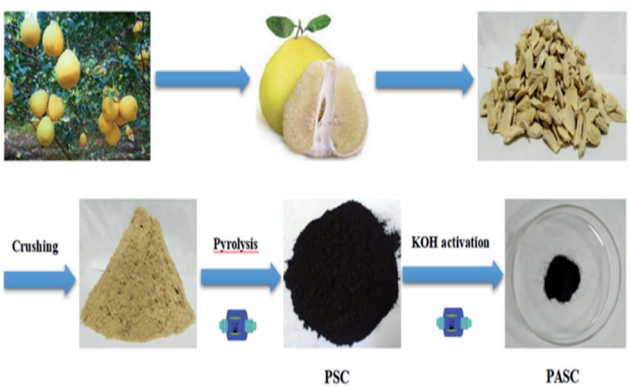

Scheme 1 Synthesis of porous carbon from waste pomelo seeds.

2.3 Electrochemical measurements

For the two-electrode system, a homogeneous slurry of the electroactive material, polytetrafluoroethylene (PTFE), and acetylene black with a weight ratio of 80 : 10 : 10 in ethanol was prepared and pasted on a nickel foam current collector (1 cm × 1 cm), and then vacuum dried at 80 °C for 12 h. The loading of the active material for each working electrode was measured to be ~3 mg cm^{-2}. And then, a piece of glass-fiber filter paper (Waterman, GF/B) as a separator and 1 M KOH aqueous solution as the electrolyte were used to assemble a test cell. For the three-electrode system, the working electrode was manufactured *via* the dispersion of active carbon in a mixture of Nafion and ethanol (1 : 20) and dropping on a glassy carbon electrode, accompanied by platinum foil Hg/HgO as the counter and reference electrodes, respectively. Electrochemical characterization was carried out on an electrochemical workstation (Shanghai Chenhua Instrument Co. Ltd, China).

For the two-electrode system, the gravimetric specific capacitance of a single electrode is calculated using the following equation:

$$C_{sp} = 2I \times \Delta t/m \times \Delta V \quad (1)$$

where C_{sp} (F g^{-1}) is the specific capacitance based on the mass of the active carbon, I is the discharge current (A), Δt is the discharge time (s), ΔV is the voltage difference (except the ohm drop) within Δt (V), and m is the loading of the active material in each working electrode (g).

For the three-electrode system, the gravimetric specific capacitance can be calculated using the following equation:

$$C_{sp} = I \times \Delta t/m \times \Delta V \quad (2)$$

where I is the discharge current (A), Δt is the discharge time (s), ΔV is the voltage (V), and m is the mass of the active materials (g).

The energy density E (W h kg^{-1}) and the power density P (W kg^{-1}) are calculated using the following equations:

$$E = C_{sp}V^2/(2 \times 3.6) \quad (3)$$

$$P = 3600E/\Delta t \quad (4)$$

where t is the discharge time (s).

3. Results and discussion

3.1 Materials characterization

As shown in Fig. 1a and b, scanning electron microscopy (SEM) and transmission electron microscopy (HRTEM) were applied to confirm the morphology and microstructure of the representative carbon activated at 800 °C. The SEM image of PSAC-3 (Fig. 1a) indicates regularly shaped particles and interconnected quasi-spherical carbon particles with a predominant diameter of 300 nm, which is homogeneous within the whole sample. Further, 3D porous channels and voids also could be formed by means of the aggregation of the homogeneous carbon particles. According to the TEM image (Fig. 1b and S1†), the mesoporous structure is distributed in the entire sample. The amorphous,

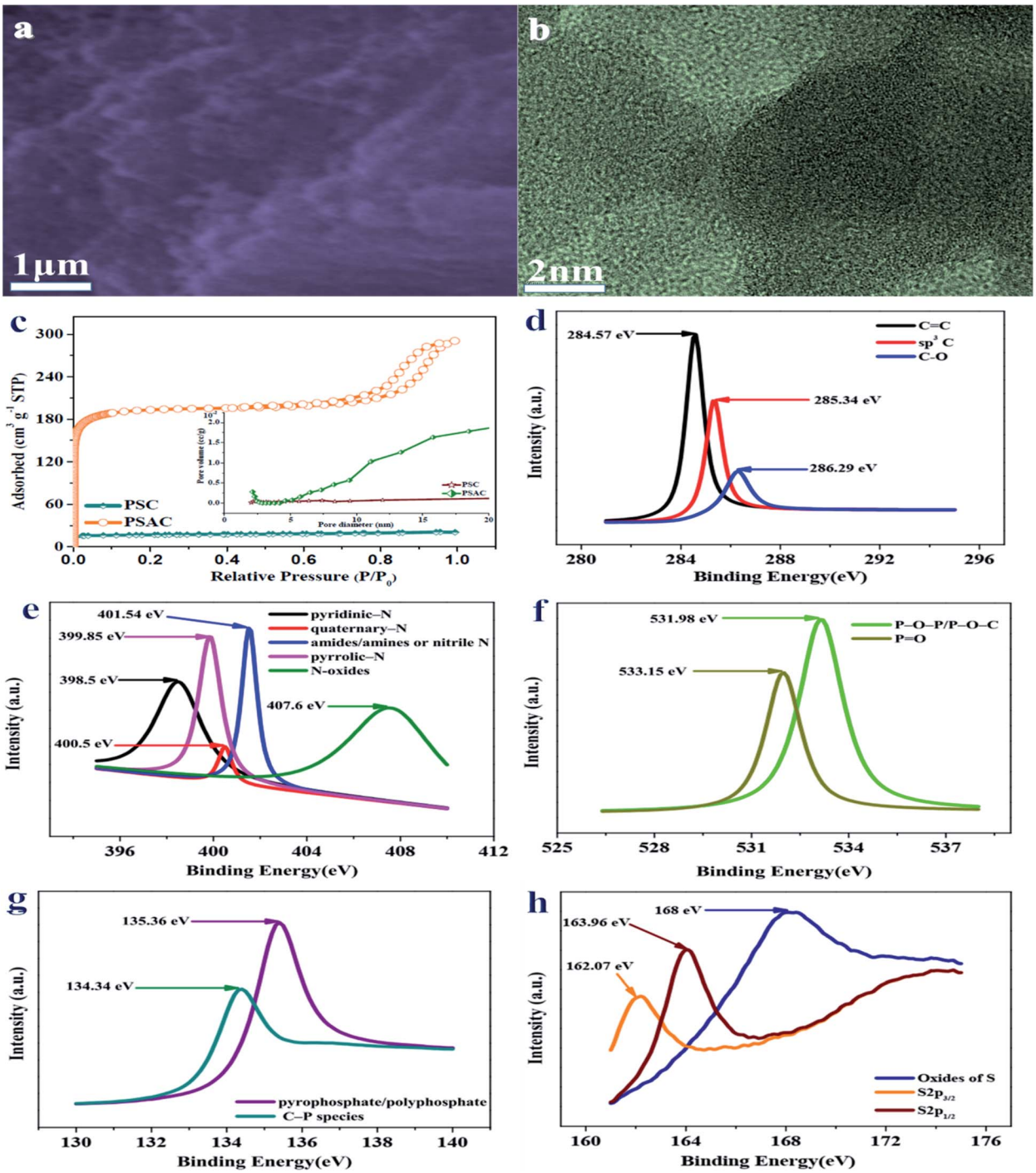

Fig. 1 (a) FESEM image of PSAC-3. (b) TEM image of PSAC-3. (c) N_2 adsorption/desorption isotherms and the pore size distribution of PSC and PSAC-3. (d) High resolution C 1s of PSAC-3. (e) High resolution N 1s of PSAC-3. (f) High resolution O 2p of PSAC-3. (g) High resolution P 2p of PSAC-3. (h) High resolution S 2p of PSAC-3.

highly disordered carbon structure for PSAC-3 is also observed. Moreover, the surface of PSAC-3 has a highly curved surface texture owing to the formation of microporous polymers, which could be further confirmed by the existence of broad XRD reflections between 20 and 25°.

The X-ray diffraction (XRD) patterns (Fig. S2†) of the as-synthesized samples demonstrate two characteristic peaks located at 2θ of ~23° and ~43°, which correspond to the (002) and (100) planes of graphitic carbon layers, respectively.[24] The broad diffraction peak of carbon is attributed to the abundant micropores in the samples. From the spectra of PSAC-3 and PSC, it could be deduced that the activation of KOH could contribute to increasing porosity as the spectra of PASC-3 show a broader peak.[25] The Raman spectra of PSAC-3 in Fig. S3† indicate two peaks located at about ~1342 cm^{-1} and ~1591 cm^{-1}, corresponding to D (disordered carbon) and G (graphitic carbon).[26] The G band originates from graphitic in-plane stretching from sp^2 carbon and the D band corresponds to defects and disorders in the carbon structure by virtue of disordered carbon atoms with dangling bonds. Owing to the activation of KOH, the I_D/I_G ratio obviously increases from 0.99 for PSC to 1.02 for PSAC-3, revealing that the graphitization intensity gradually becomes weaker, which agrees well with the XRD analysis and TEM images.

The porosity parameters of these carbon samples are further characterized by N_2 adsorption/desorption isothermal analysis (Fig. 1c), and the relevant data are listed in Table 1. The isotherm of PAC is type I, indicating the microporous nature of the carbon with a surface area of ~58 $m^2\ g^{-1}$ and a pore volume of 0.032 $cm^{-3}\ g^{-1}$. PSAC-3 also shows a type I isotherm owing to strong adsorption on micropores, followed by a H4 hysteresis due to the presence of mesopores. The BET surface area of PSAC-3 is calculated to be ~1187 $m^2\ g^{-1}$ with a pore volume of 0.616 $cm^{-3}\ g^{-1}$. As shown by the DFT pore size distribution curve (inset in Fig. 1c), most pores are smaller mesopores of less than 10 nm in size, with major pores ranging from 2 to 5 nm (Fig. S4†). The average pore sizes of PSAC-3 and PSC are 2.91 nm and 2.503 nm, respectively. The activation of KOH could contribute to increasing the textural properties and further maximizing the ion adsorption sites, due to the generation of a huge amount of gases (CO and CO_2) from the activation agent (KOH).[27] According to the effect of the activation temperature, the BET surface area and the pore volume as well as the average pore size of PSAC-6 (700 °C) and PSAC-7 (900 °C) are 488.999 $m^2\ g^{-1}$, 0.416 $cm^{-3}\ g^{-1}$, 2.365 nm; 673 $m^2\ g^{-1}$, 0.448 $cm^{-3}\ g^{-1}$, 2.91 nm, respectively. With the increase of the activation temperature from 700 °C to 800 °C, the textural properties similarly increase. However, when the activation temperature further increases to 900 °C, the pores may collapse, which unfavorably results in the decrease of the textural properties. Therefore, PSAC-3 could effectively favor fast ion movement and accommodation of large solvated ions, further leading to high capacitance and providing quick electrolyte diffusion into deeper pores.[28]

The chemical nature of the as-synthesized samples is further characterized by FT-IR in the 500–4000 cm^{-1} region. As described in Fig. S5,† the strong peak at 3443 cm^{-1} is typically due to the O–H stretching vibration (hydroxyl groups and chemisorbed water) and/or N–H symmetric stretching vibration.[29] The bands at 2977 cm^{-1} are due to the C–H stretching vibrations. The bands at 1669 cm^{-1} are attributed to the stretching vibration of C=O (COOH functional groups). The spectra at 1469 cm^{-1} and 1321 cm^{-1} are ascribed to the deformation vibrations of C–H and O–H, respectively. The signal located at 1040 cm^{-1} is assigned to C–O–C (symmetric angular deformation of ethers).[30] Hence, the FT-IR analysis indicates the existence of nitrogen and oxygen species in the as-synthesized porous ACs.

The chemical compositions of pomelo seed-derived carbon are characterized by XPS. Carbon, nitrogen, oxygen, phosphorus and sulphur are detected in PSAC-3. The corresponding high-resolution XPS spectra of PSAC-3 are presented in Fig. 1d–h. All of them are essential elements in biomass components, *e.g.*, nitrogen from proteins and phosphorus from nucleic acids. In the high-resolution XPS C 1s spectrum (Fig. 1d), 3 major peaks at 284.57, 285.34 and 286.29 eV correspond to the C=O bond, sp^3 carbon and C–O bond, respectively.[31] As shown in Fig. 1e, the deconvolution of N 1s demonstrates 5 major sub-peaks at 398.5, 399.85, 400.5, 401.54 and 407.6 eV, which can be attributed to the binding energies of pyridinic, pyrrolic, quaternary, amides/amines and nitrile and pyridinic oxide types of nitrogen.[32,33] In the O 2p XPS spectrum (Fig. 1f), two peaks deconvoluted for the O 1s spectra at 531.98 and 533.15 eV are assigned to P–O–P/P–O–C linkages and P=O groups,

Table 1 Summary of BET characteristics of activated carbons

Sample	S_{BET}[a] ($m^2\ g^{-1}$)	V_{tot}[b] ($cm^3\ g^{-1}$)	S_{mic}[c] ($m^2\ g^{-1}$)	S_{me}[d] ($m^2\ g^{-1}$)	S_{ma}[e] ($m^2\ g^{-1}$)	V_{mic}[f] ($cm^3\ g^{-1}$)	V_{me}[g] ($cm^3\ g^{-1}$)	V_{ma}[h] ($cm^3\ g^{-1}$)
PSC	57.998	0.032	3.67	43.28	11.048	0.0062	0.0238	0.002
PSAC-1	245.82	0.135	86.132	105.62	54.068	0.0138	0.0461	0.0751
PSAC-2	1432.125	0.718	349.06	969.377	113.688	0.175	0.486	0.058
PSAC-3	1187.439	0.616	313.62	668.53	205.289	0.162	0.346	0.108
PSAC-4	373.664	0.144	121.56	134.89	117.214	0.319	0.157	0.255
PSAC-5	436.087	0.400	93.72	236.26	106.107	0.085	0.216	0.099
PSAC-6	488.999	0.416	98.42	261.68	128.899	0.083	0.249	0.084
PSAC-7	672.756	0.448	103.56	412.73	156.466	0.068	0.274	0.106

[a] S_{BET}: BET surface area. [b] V_{tot}: total volume. [c] S_{mic}: micropore surface area. [d] S_{me}: mesopore surface area. [e] S_{ma}: macropore surface area. [f] V_{mic}: micropore volume. [g] V_{me}: mesopore volume. [h] V_{ma}: macropore volume.

respectively.[34] According to the P 2p XPS spectrum (Fig. 1g), the two peaks at 134.34 eV and 135.36 eV could be ascribed to C–P species and pyrophosphate/polyphosphate (PP),[35] respectively. In the S 2p XPS spectrum (Fig. 1h), three peaks at 162.07 eV, 163.96 eV and 168 eV could be detected and attributed to S $2p_{3/2}$ (C═S), S $2p_{1/2}$ (C–S) and oxides and S,[36] respectively.

3.2 Electrochemical behavior of the electrode

Owing to the unique structure of the PSAC, including the interconnected hierarchical porous structure (micro- and mesopores) and the high porosity (~1187 $m^2\ g^{-1}$) obtained *via* chemical activation, PSAC materials have potential for application as innovative electrode materials for supercapacitors. In order to demonstrate this viewpoint, we investigate the electrochemical capacitance of all PSAC-derived materials in a three-electrode configuration in 1 M KOH solution. The cyclic voltammetry (CV) curves are recorded first at a standard scan rate of 100 mV s^{-1} to get a glance of the electrochemical behavior of all materials. According to the CV curves in Fig. S6a–c,† PSAC-3 encloses the largest area among the sample materials, which confirms the highest capacitance.[37] Meanwhile, the CV curves of PSAC-3 maintain a quasi-rectangular shape with subtle broadened humps, revealing dominant electric double-layer capacitance behavior with a strong synergistic effect of reversible pseudocapacitance from the limited surface oxygen groups.[38] The appearance of humps in the CV curves indicates

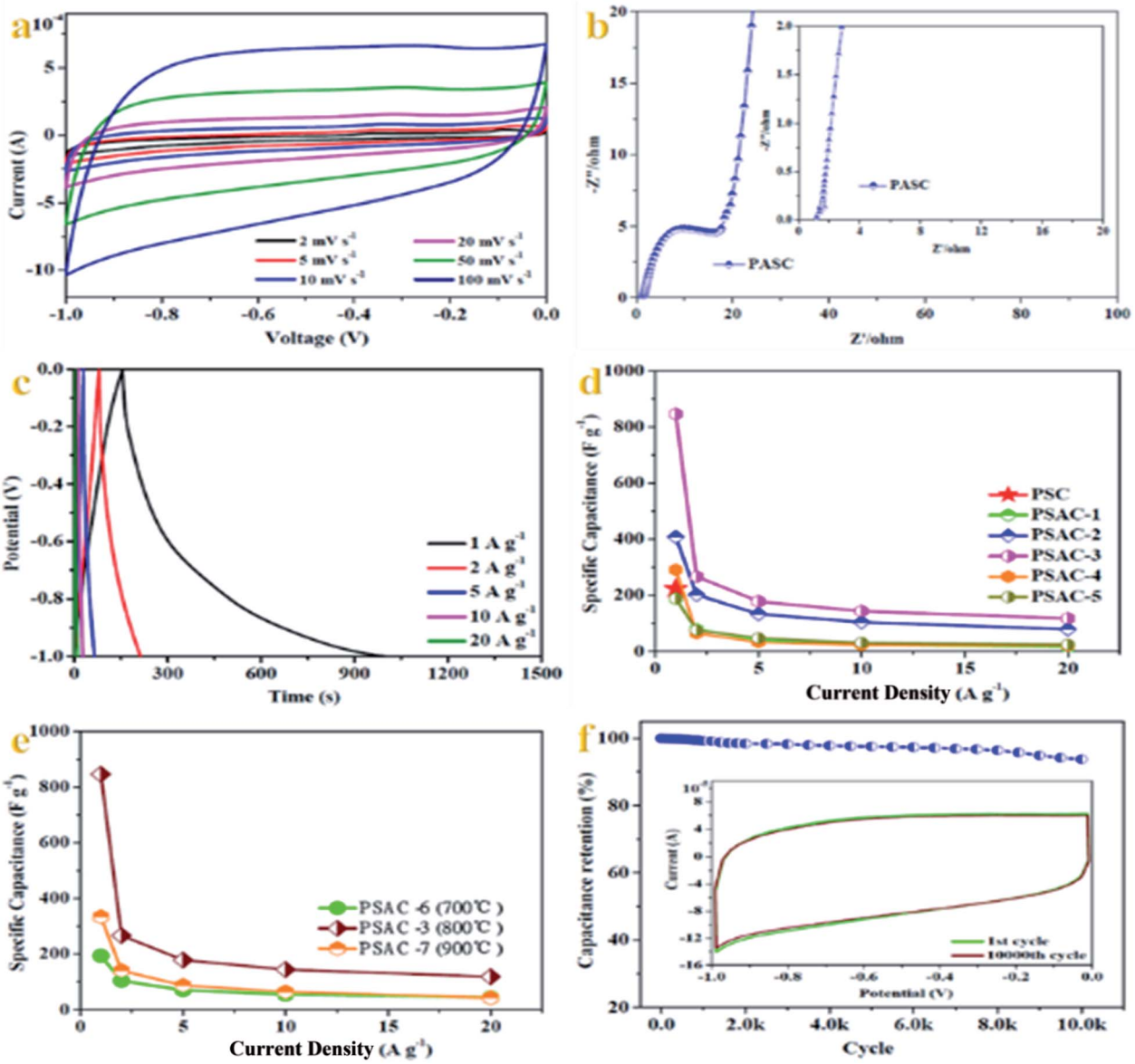

Fig. 2 (a) CV curves of PSAC-3 at different scan rates. (b) Nyquist plots of PSAC-3. (c) Galvanostatic charge/discharge curves of PSAC-3 at different current densities. (d) Capacitances of PSAC samples prepared with different ratios of precursor/KOH at different current densities. (e) Capacitances of PSAC samples prepared at different temperatures at different current densities. (f) Cycling performance of PSAC-3 at 10 A g^{-1}. The inset shows the CV curves of the 1st and 10 000th cycle.

the presence of pseudocapacitance, which is related to surface oxygen and nitrogen functional groups.[39] Furthermore, the CV curves for PSAC-3 (Fig. 2a) at various scan rates from 5 to 100 mV s^{-1} indicate that the nearly rectangular shape is maintained at a low scan rate of below 50 mV s^{-1} implying relatively high rate capability. However, the characteristics are slightly aggravated at 100 mV s^{-1}. Such limitations at higher scan rates demonstrate that faradaic reactions take place during charge transport.[40]

As shown in Fig. 2b, the electrochemical impedance spectroscopy (EIS) of PSAC-3 presents a semicircular shape in the high frequency region and the line is approximately vertical in the low frequency region. Obviously, the slopes of PSAC-3 in the low frequency region are all almost close to 90°, which further confirms the ideal capacitive behavior as an electrode material. PSAC-3 also exhibits a low intercept (1.16 Ω, 106.338 kHz) on the real axis due to the surface wettability derived from the coexistence of nitrogen and oxygen.[41] Moreover, a 45° Warburg impedance and nearly vertical curves of Nyquist plots at low frequency imply the ideal capacitance behavior, which further confirms that PSAC-3 is an excellent electrode material for supercapacitors.[42]

To further investigate the performance of the prepared samples, GCD experiments are performed at different current densities utilizing the same voltage windows as for the CV test. As shown in Fig. 2c, the GCD curves for PSAC-3 indicate almost linear and symmetrical curves, which confirm the superior electrochemical reversibility and coulombic efficiency.[43] Based on the discharge curves, PSAC-3 exhibits a specific capacitance of 845.50 F g^{-1} at 1 A g^{-1}, which is much higher than that of PSC (~223 F g^{-1}). Moreover, specific capacitances of ~266, ~178, ~144, and ~118 F g^{-1} are also achieved at current densities of 2, 5, 10 and 20 A g^{-1}, respectively. The decrease of capacitance at higher current is generally attributed to increased ohmic resistance due to the ion "traffic jam" within the particles' micropores or due to the interaction of electrolyte with carbon functional groups or dangling bonds.[44] The results are also superior to those for many other carbonaceous capacitive materials derived from biomass,[45–48] which agrees well with the results obtained from CV tests. As the amount of KOH activating agent is increased, the specific capacitance increased until reaching an optimum value, beyond which it drastically decreased again. It is evident from Fig. 2d that the PSAC samples display an increase in their specific capacitances with the decrease of the ratio of PSC to KOH (2 : 1 *vs.* 3 : 2 *vs.* 1 : 1, 188.63 *vs.* 408.07 *vs.* 845.50 F g^{-1} at 1 A g^{-1}; PSAC-1 *vs.* PSAC-2 *vs.* PSAC-3). However, the specific capacitances for the PSAC samples also progressively decreased with the decrease of the ratio of PSC to KOH (1 : 1 *vs.* 2 : 3 *vs.* 1 : 2, 845.50 *vs.* 290.40 *vs.* 188.03 F g^{-1}, PSAC-3 *vs.* PSAC-4 *vs.* PSAC-5). In addition, the specific capacitance of PSAC-3 at 800 °C (Fig. 2e) obviously exceeds that of PSAC-6 (700 °C) and PSAC-7 (900 °C) (800 *vs.* 700 *vs.* 900 °C, 845.50 *vs.* 193.00 *vs.* 333.70 F g^{-1} at 1 A g^{-1}; PSAC-3 *vs.* PSAC-6 *vs.* PSAC-7), owing to the higher surface area and large pore size of the former, which favor the kinetics of the ion adsorption process.[49] In general, PSAC-3 has a higher surface area with a uniform pore size distribution which facilitates faster ion movement, which in turn increases the specific capacitance.

The cycling stability is evaluated by the continuous charge–discharge process with a current density of 10 A g^{-1}. As expected, PSAC-3 shows a smooth trend and presents a high capacitance retention of 93.8% after 10 000 cycles, further suggesting that the cooperation between appropriate pore distribution and rational structure results in the superb electrochemical stability and outstanding reversibility of the PSAC-3 electrode.[50] Notably, the GCD curve of the 10 000th cycle retains an almost identical shape to that of the 1st cycle by maintaining its linearity and symmetry, highlighting the excellent reversibility and long-term electrochemical stability (inset in Fig. 2f).

3.3 Supercapacitor performance

The electrochemical performance of PSAC-3 based supercapacitors is evaluated in a fully assembled two-electrode cell with 1 M KOH electrolyte. As shown in Fig. 3a, the CV curves of the supercapacitors at different scan rates varying from 5 to 100 mV s^{-1} present quasi-rectangular-like shapes with no obvious distortion, which confirms the EDLC capacitive performance.[51] However, the curves are deformed with an increase of the scan rate by virtue of the slow charge–discharge kinetics of PSAC-3 materials in the KOH electrolyte. And further ion diffusion could not adequately access the surface of PSAC-3 in such a short time at high scan rates.[52]

The Nyquist plots of the device (Fig. 3b) indicate a small impedance of 2.39 Ω (6.17 kHz) with a vertical line in the low-frequency region, demonstrating the fast and efficient ionic transport in the KOH electrolyte.[53] Moreover, the GCD curves exhibit regularly triangular shapes with no distinct voltage drop in the whole voltage window of 0–1.2 V (Fig. 3c), suggesting a low internal resistance and a good electrochemical reversibility. Low equivalent series resistance (ESR) of the assembled devices has also been proved by their low IR drops (voltage drops).[54] Fig. 3d shows the comparison of the capacitance of the device in the current density range from 1 to 10 A g^{-1}, which gives rise to the change of capacitance from ~426 to ~343 F g^{-1}, demonstrating a good rate performance. The specific capacitance is still as high as 310 F g^{-1} with a retention of 72.8% at a high current density of 20 A g^{-1}, which could be attributed to the interconnected structure with developed hierarchical porosity, contributing to rapid electrolyte transfer and enhanced degree of graphitization, which imparts good electrical conductivity.[55] With the increase of current density (Fig. 3d), the capacitance values show a slightly decreased trend due to the steric limitations of materials over which ions can only partially penetrate into the micropores.[56] The Ragone plot of the device in KOH electrolyte calculated from discharge curves at different current densities is displayed in Fig. 3e. The maximum energy density of the device is up to ~85 W h kg^{-1} at a power density of 1.2 kW kg^{-1}. As is known, the energy density is suppressed with the increase of current density since the limited pores on the surface are accessed by electrolyte ions for fast discharging at high current density, whereas almost all pores could be utilized at a low current density.[57] Nonetheless, it

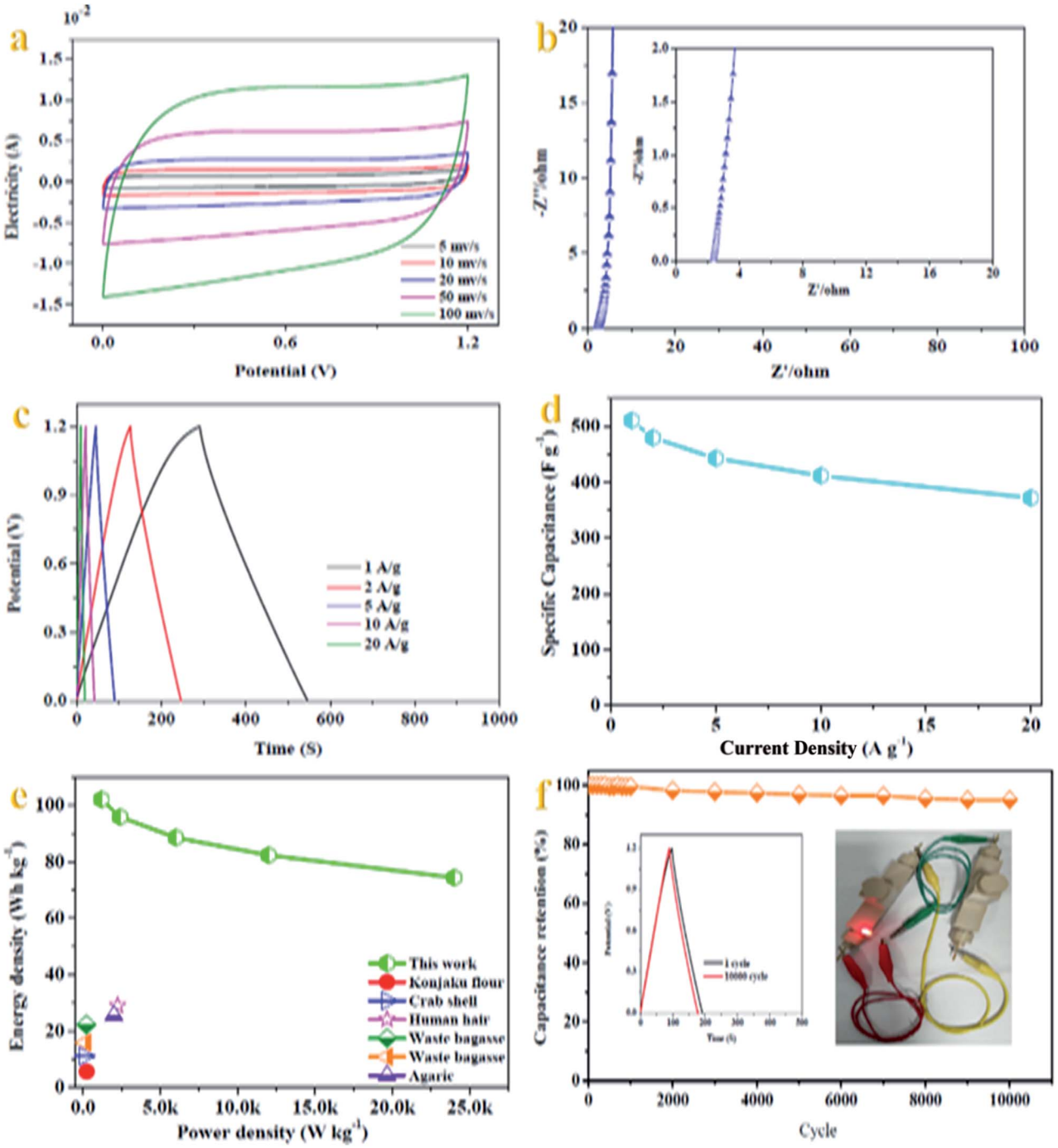

Fig. 3 (a) CV curves of the PSAC//PSAC symmetrical supercapacitor at different scan rates in the voltage window of 0–1.2 V. (b) Nyquist plots of the PSAC//PSAC symmetrical supercapacitor. (c) Galvanostatic charge/discharge curves of the PSAC//PSAC symmetrical supercapacitor at different current densities. (d) Specific capacitances of the as-assembled PSAC symmetrical supercapacitor based on the total mass of the active materials of the two electrodes at different current densities. (e) Ragone plots of the PSAC symmetrical supercapacitor and other previously reported carbon-based symmetric supercapacitors. (f) Cycling performance of the PSAC symmetrical supercapacitor at a current density of 10 A g^{-1} (inset shows the photograph of the GCD curves for recycling and lighting LED bulbs).

is noteworthy to mention that the energy density still reached 62 W h kg^{-1} with a power density of 24 kW kg^{-1} at a current density of 20 A g^{-1}, which is higher than those of commercially available supercapacitors (3–5 W h kg^{-1}) and other previously reported biomass-derived heteroatom-doped carbonaceous symmetric supercapacitors.[58–62]

Notably, the PSAC-based symmetric supercapacitor shows about 95.04% retention of its initial capacitance after 10 000 charge and discharge cycles at a current density of 10 A g^{-1} (Fig. 3f), verifying an outstanding durability and long-term cycling stability. The hierarchical porous structure, excellent pore stability, enhanced wettability and good conductivity are

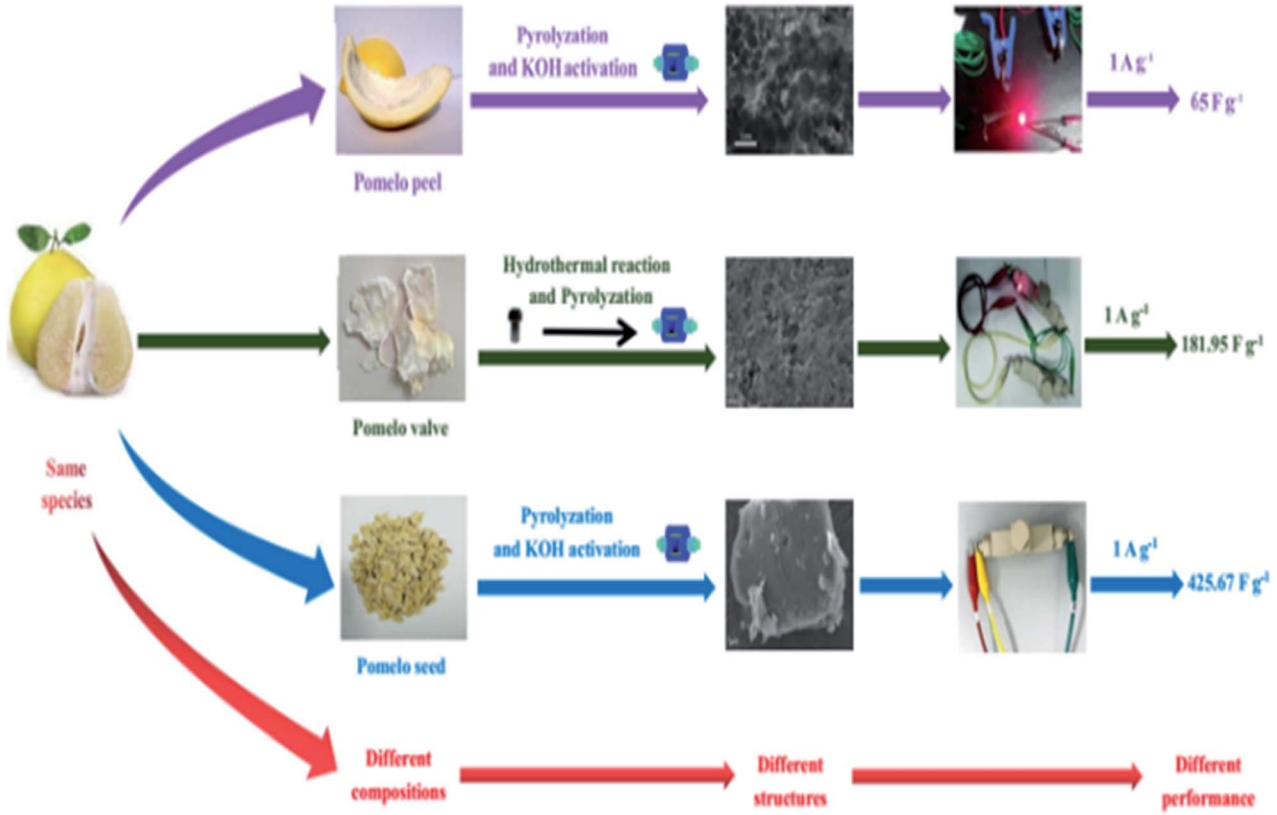

Fig. 4 Effect of different ingredients derived from pomelo on the performance of the supercapacitor.

responsible for the outstanding cycling performance.[63] Meanwhile, the GCD curves in the 1st and 10 000th cycle at 1 A g^{-1} are almost fully overlapped except a faint decay, which is similar to the CV curves and Nyquist plots of the devices before and after recycling (Fig. S7a and b†), demonstrating the perfect pore structure stability of the obtained materials. Moreover, the hierarchical porous structure can facilitate ion diffusion in the bulk carbon structure.[64] A rational combination of different size pores can improve specific capacitance, rate capability, and cycling performance, which are central to the success of porous carbons for charge storage applications.[65,66] To further meet the practical application requirements for modern wearable and portable energy storage devices, a tandem device is assembled by connecting two prototype units in series. And then, the device is used to light up a red light-emitting-diode (LED, the lowest working potential is 2.0 V), as depicted in the inset of Fig. 3f. This tentative test confirms that the facile and cost-efficient synthesis strategy for designing analogous biomass-derived materials such as PSAC-3 paves the way for a new direction for expanding their practical applications in energy storage and conversion.

In addition, the waste raw materials derived from pomelo such as pomelo peel and pomelo valves have been used to fabricate porous carbon for supercapacitors. The specific capacitances of the devices with pomelo peel and pomelo valve-based electrodes[67,68] are 68 F g^{-1} at 0.2 A g^{-1} and ~182 F g^{-1} at 1 A g^{-1}.

Based on the results, the different performances are presented according to the different parts of pomelo, owing to different ingredients. The components of pomelo peel mainly include naringin and neohesperidin. Pomelo seeds are mainly composed of fatty oil and obacunone as well as obakulactone (Fig. 4). Above all, the difference in composition and content could also play a vital role in the performance, even for the different components of the same species.

4. Conclusions

In summary, a heteroatom-doped porous carbon with an ultrathin nanosheet structure is derived from pomelo seeds by a one-step pyrolysis and activation process. The as-synthesized carbon materials have abundant micropores with a super high surface area of ~1187 m^2 g^{-1} and a pore volume of 0.616 cm^3 g^{-1}, which contributes to a high specific capacitance of 845.50 F g^{-1} at a current density of 1 A g^{-1}. This type of PSAC serves very well as electrodes in 1.2 V aqueous supercapacitors, presenting a high specific capacitance of ~426 F g^{-1} at 1 A g^{-1} and an energy density of ~85 W h kg^{-1} at a power density of 1.2 kW kg^{-1} as well as an outstanding electrochemical stability (only a 4.96% capacitance loss after 10 000 cycles). Therefore, this work provides a facile strategy to synthesize a porous carbon with moderate surface area and excellent electrochemical performance, which is a promising material for supercapacitors, adsorbents, and catalysts.

Conflicts of interest

There are no conflicts to declare.

Acknowledgements

We gratefully acknowledge the financial support from the Faculty of Materials and Energy and Institute for Clean Energy & Advanced Materials, Southwest University, and Chongqing Key Laboratory for Advanced Materials and Technologies of Clean Electrical Power Sources and this work is sponsored by the Natural Science Foundation of Chongqing, China (cstc2020jcyj-msxmX0019).

References

1 L. Yang, L. Song, Y. Feng, M. Cao, P. Zhang, X. Zhang and J. Yao, *J. Mater. Chem. A*, 2020, **8**, 12314.
2 S. L. Mei, X. H. Xu, R. D. Priestley and Y. Lu, *Chem. Sci.*, 2020, **11**, 12269.
3 E. Temeche, M. Yu and R. M. Laine, *Green Chem.*, 2020, **22**, 4656.
4 M. L. Mao, Z. Yu, Z. j. Lin, Y. S. Hu, H. Li, X. j. Huang, L. Q. Chen, M. Liu and L. M. Suo, *J. Mater. Chem. A*, 2020, **8**, 23834.
5 K. Zhou, Y. He, Q. C. Xu, Q. E. Zhang, A. A. Zhou, Z. H. Lu, L. K. Yang, Y. Jiang, D. T. Ge, X. Y. Liu and H. Bai, *ACS Nano*, 2018, **12**, 5888.
6 Y. L. Zhu, W. Du, Q. L. Zhang, H. Yang, Q. Zong, Q. Q. Wang, Z. Zhou and J. H. Zhan, *Chem. Commun.*, 2020, **56**, 13848.
7 F. Yi, H. Ren, K. Dai, X. Wang, Y. Han, K. Wang, K. Li, B. Guan, J. Wang, M. Tang, J. Shan, H. Yang, M. Zheng, Z. You, D. Wei and Z. Liu, *Energy Environ. Sci.*, 2018, **11**, 2016.
8 K. Hassan, M. J. Nine, T. T. Tung, N. Stanley, P. L. Yap, H. Rastin, L. Yu and D. Losic, *Nanoscale*, 2020, **12**, 19007.
9 Z. Bi, Q. Kong, Y. Cao, G. Sun, F. Su, X. Wei, X. Li, A. Ahmad, L. Xie and C. Chen, *J. Mater. Chem. A*, 2019, **7**, 16028.
10 C. Z. Sun, Y. D. Ruan, W. P. Zha, W. W. Li, M. L. Cai and Z. Y. Wen, *Mater. Horiz.*, 2020, **7**, 1667.
11 Y. Y. Zhang, J. J. He, Z. Gao and X. D. Li, *Nano Energy*, 2019, **65**, 104045.
12 R. Sahoom, T. Lee, D. Pham, T. Luu and Y. Lee, *ACS Nano*, 2019, **13**, 10776.
13 J. Wu, Q. Zhang, J. Wang, X. Huang and H. Bai, *Energy Environ. Sci.*, 2018, **11**, 1280.
14 F. C. Zhou, Z. W. Ren, Y. D. Zhao, X. P. Shen, A. W. Wang, Y. Y. Li, C. Surya and Y. Chai, *ACS Nano*, 2016, **10**, 5900.
15 M. H. Yu, Z. F. Wang, H. Z. Zhang, P. P. Zhang, T. Zhang, X. H. Lu and X. L. Feng, *Nano Energy*, 2019, **65**, 103987.
16 B. Li, F. Dai, Q. Xiao, L. Yang, J. Shen, C. Zhang and M. Cai, *Adv. Energy Mater.*, 2016, **6**, 1600802.
17 S. Zhang, L. N. Sui, H. Z. Dong, W. B. He, L. F. Dong and L. Y. Yu, *ACS Appl. Mater. Interfaces*, 2018, **10**, 12983.
18 X. Peng, L. Zhang, Z. Chen, L. Zhong, D. Zhao, X. Chi, X. Zhao, L. Li, X. Lu, K. Leng, C. Liu, W. Liu, W. Tang and K. Loh, *Adv. Mater.*, 2019, **31**, 1900341.
19 Y. G. Wang, Y. F. Song and Y. Y. Xia, *Chem. Soc. Rev.*, 2016, **45**, 5925.
20 Z. Wang, A. T. Smith, W. Wang and L. Sun, *Angew. Chem., Int. Ed.*, 2018, **57**, 13722.
21 X. Dong, H. Jin, R. Wang, J. Zhang, X. Feng, C. Yan, S. Chen, S. Wang, J. Wang and J. Lu, *Adv. Energy Mater.*, 2018, **8**, 1702695.
22 Y. Zhang, M. Y. Xie, V. Adamaki, H. Khanbareh and C. R. Bowen, *Chem. Soc. Rev.*, 2017, **46**, 7757.
23 Y. Wang, H. Guo, X. Luo, X. Liu, Z. Hu, L. Han and Z. Zhang, *Small*, 2019, **15**, 1805277.
24 R. R. Cessa, H. Grebel, Z. Jiang, C. Fukuda, H. Pita, T. S. Chowdhury, Z. Dong and Y. Wan, *Environ. Prog. Sustainable Energy*, 2018, **37**, 155.
25 N. Choudhary, C. Li, J. Moore, N. Nagaiah, L. Zhai, Y. Jung and J. Thomas, *Adv. Mater.*, 2017, **29**, 1605366.
26 Y. Liu, B. Huang, X. Lin and Z. Xie, *J. Mater. Chem. A*, 2017, **25**, 13009.
27 Z. Yu, L. Tetard, L. Zhai and J. Thomas, *Energy Environ. Sci.*, 2015, **3**, 702.
28 B. Chang, W. Shi, S. Han, Y. Zhou, Y. Liu, S. Zhang and B. Yang, *Chem. Eng. J.*, 2018, **350**, 585.
29 S. Gao, X. Li, L. Li and X. Wei, *Nano Energy*, 2017, **33**, 334.
30 Y. Gong, D. Li, C. Luo, Q. Fu and C. Pan, *Green Chem.*, 2017, **19**, 4132.
31 C. Zu and A. Manthiram, *Adv. Energy Mater.*, 2013, **3**, 1008.
32 T. Palaniselvam, M. O. Valappil, R. Illathvalappil and S. Kurungot, *Energy Environ. Sci.*, 2014, **7**, 1059.
33 M. Cheng, Y. Meng, Q. Meng, L. Mao, M. Zhang, K. Amin, A. Ahmad, S. Wu and Z. Wei, *Mater. Chem. Front.*, 2018, **2**, 986.
34 M. L. Sánchez, A. Primo and H. García, *Angew. Chem., Int. Ed.*, 2013, **52**, 11813.
35 R. Huang, J. Wang, B. Zhang, K. H. Wu, Y. Zhang and D. S. Su, *Catal. Sci. Technol.*, 2018, **8**, 1522.
36 D. Mohapatra, G. Dhakal, M. S. Sayed, B. Subramanya, J. Shim and S. Parida, *ACS Appl. Mater. Interfaces*, 2019, **11**, 8040.
37 Y. Shao, M. F. E. Kady, J. Sun, Y. Li, Q. Zhang, M. Zhu, H. Wang, B. Dunn and R. B. Kaner, *Chem. Rev.*, 2018, **118**, 9233.
38 S. Dong, X. He, H. Zhang, X. Xie, M. Yu, C. Yu, N. Xiao and J. Qiu, *J. Mater. Chem. A*, 2018, **6**, 15954.
39 Y. Huang, H. Li, Z. Wang, M. Zhu, Z. Pei, Q. Xue, Y. Huang and C. Zhi, *Nano Energy*, 2016, **22**, 422.
40 R. Thangavel, A. G. Kannan, R. Ponraj, V. Thangavel, D. W. Kim and Y. S. Lee, *J. Mater. Chem. A*, 2018, **6**, 17751.
41 Y. Zhang, J. He, Z. Gao and X. Li, *Nano Energy*, 2019, **65**, 104045.
42 J. Niu, R. Shao, J. Liang, M. Dou, Z. Li, Y. Huang and F. Wang, *Nano Energy*, 2017, **36**, 322.
43 M. Yu, Z. Wang, H. Zhang, P. Zhang, T. Zhang, X. Lu and X. Feng, *Nano Energy*, 2019, **65**, 103987.
44 W. Qian, F. Sun, Y. Xu, L. Qiu, C. Liu, S. Wang and F. Yan, *Energy Environ. Sci.*, 2014, **7**, 379.
45 A. Noori, M. F. E. Kady, M. S. Rahmanifar, R. B. Kaner and M. F. Mousavi, *Chem. Soc. Rev.*, 2019, **48**, 1272.

46 F. Wang, X. Wu, X. Yuan, Z. Liu, Y. Zhang, L. Fu, Y. Zhu, Q. Zhou, Y. Wu and W. Huang, *Chem. Soc. Rev.*, 2017, **46**, 6816.
47 M. Yuan, X. Guo, Y. Liu and H. Pang, *J. Mater. Chem. A*, 2019, **7**, 22123.
48 W. J. Liu, H. Jiang and H. Q. Yu, *Energy Environ. Sci.*, 2019, **12**, 1751.
49 Y. Zhang, X. Liu, S. Wang, L. Li and S. Dou, *Adv. Energy Mater.*, 2017, **7**, 1700592.
50 H. Wang, Y. Yang and L. Guo, *Adv. Energy Mater.*, 2017, **7**, 1700663.
51 B. Zhu, B. Liu, C. Qu, H. Zhang, W. Guo, Z. Liang, F. Chen and R. Zou, *J. Mater. Chem. A*, 2018, **6**, 1523.
52 Z. Bi, Qi. Kong, Y. Cao, G. Sun, F. Su, X. Wei, X. Li, A. Ahmad, L. Xie and C. M. Chen, *J. Mater. Chem. A*, 2019, **7**, 16028.
53 R. Mo, F. Li, X. Tan, P. Xu, R. Tao, G. Shen, X. Lu, F. Liu, L. Shen, B. Xu, Q. Xiao, X. Wang, C. Wang, J. Li, G. Wang and Y. Lu, *Nat. Commun.*, 2019, **10**, 1474.
54 J. Gao, G. Wang, Y. Liu, J. Li, B. Peng, S. Jiao, S. Zeng and G. Zhang, *J. Mater. Chem. A*, 2020, **8**, 13946.
55 Q. Cai, J. Mao, Y. Li, J. Liu, H. Zhang, J. Huang, T. Wu, Y. Yang, C. Yuan and L. Dai, *J. Mater. Chem. A*, 2020, **8**, 14254.
56 H. Lv, X. Zhang, F. Wang, G. Lv, T. Yu, M. Lv, J. Wang, Y. Zhai and J. Hu, *J. Mater. Chem. A*, 2020, **8**, 14287.
57 Q. Bai, Y. Shen, T. A. Asoh, C. Li, Y. Dan and H. Uyama, *Nanoscale*, 2020, **12**, 15261.
58 Y. Liu, Z. Xiao, Y. Liu and L. Z. Fan, *J. Mater. Chem. A*, 2018, **6**, 160.
59 Y. Zhang, S. Liu, X. Zheng, X. Wang, Y. Xu, H. Tang, F. Kang, Q. H. Yang and J. Luo, *Adv. Funct. Mater.*, 2017, **27**, 1604687.
60 M. Zohair, K. Moyer, J. E. Rathert, C. Meng, J. Waugh and C. L. Pint, *ACS Nano*, 2020, **14**, 2308.
61 B. Zhu, B. Liu, C. Qu, H. Zhang, W. Guo, Z. Liang, F. Chen and R. Zou, *J. Mater. Chem. A*, 2018, **6**, 1523.
62 R. Thangavel, A. G. Kannan, R. Ponraj, V. Thangavel, D. W. Kim and Y. S. Lee, *J. Mater. Chem. A*, 2018, **6**, 17751.
63 M. Sevilla and A. B. Fuertes, *ACS Nano*, 2014, **8**, 5069.
64 R. Thangavel, A. G. Kannan, R. Ponraj, X. Sun, D. W. Kim and Y. S. Lee, *J. Mater. Chem. A*, 2018, **6**, 9846.
65 A. Balducci, *J. Power Sources*, 2016, **326**, 534.
66 R. Thangavel, B. Moorthy, D. K. Kim and Y. S. Lee, *Adv. Energy Mater.*, 2017, **7**, 1602654.
67 Q. H. Liang, L. Ye, Z. H. Huang, Q. Xu, Y. Bai, F. Y. Kang and Q. H. Yang, *Nanoscale*, 2014, **6**, 13831.
68 J. Huang, J. Chen, Z. Y. Yin and J. G. Wu, *Nanoscale Adv.*, 2020, **2**, 328.